



OPEN

# Quantum interference measurement of spin interactions in a bio-organic/semiconductor device structure

SUBJECT AREAS:

PHYSICS

CONDENSED-MATTER PHYSICS

Vincent Deo<sup>1,2</sup>, Yao Zhang<sup>2</sup>, Victoria Soghomonian<sup>2</sup> & Jean J. Heremans<sup>2</sup>

Received

12 November 2014

Accepted

4 March 2015

Published

30 March 2015

Correspondence and requests for materials should be addressed to J.J.H. (heremans@vt.edu)

<sup>1</sup>Physics Department, Ecole Polytechnique, 91128 Palaiseau, France, <sup>2</sup>Department of Physics, Virginia Tech, Blacksburg VA 24061, USA.

Quantum interference is used to measure the spin interactions between an InAs surface electron system and the iron center in the biomolecule hemin in nanometer proximity in a bio-organic/semiconductor device structure. The interference quantifies the influence of hemin on the spin decoherence properties of the surface electrons. The decoherence times of the electrons serve to characterize the biomolecule, in an electronic complement to the use of spin decoherence times in magnetic resonance. Hemin, prototypical for the heme group in hemoglobin, is used to demonstrate the method, as a representative biomolecule where the spin state of a metal ion affects biological functions. The electronic determination of spin decoherence properties relies on the quantum correction of antilocalization, a result of quantum interference in the electron system. Spin-flip scattering is found to increase with temperature due to hemin, signifying a spin exchange between the iron center and the electrons, thus implying interactions between a biomolecule and a solid-state system in the hemin/InAs hybrid structure. The results also indicate the feasibility of artificial bioinspired materials using tunable carrier systems to mediate interactions between biological entities.

In a hybrid bio-organic/semiconductor lithographic structure, quantum interference experiments are used to study spin interactions between the iron center in hemin and a proximate two-dimensional electron system (2DES) at the surface of InAs. Hemin (Fig. 1a) is an iron porphyrin similar to the prosthetic heme group in hemoglobin, where the iron center impacts biological functions. In the hemin/semiconductor structure a magnetic characterization method is employed deriving its sensitivity from electrically-measured quantum interference, evidenced as electron antilocalization<sup>1</sup>, and from the engineered nanoscale proximity between the 2DES to the local spin moments in hemin. Hemin influences the spin environment of the electrons, resulting in a temperature-dependence of the electron spin-flip scattering. Here we demonstrate that the influence of the spin environment on the decoherence times of low-dimensional electrons can be electronically measured in a bio-organic/semiconductor device to characterize a biomolecule. The approach is in principle similar to magnetic resonance techniques in its use of decoherence times, but is implemented electronically.

The 2DES in this study is the electron accumulation layer at the surface of (001) InAs, schematically represented in Fig. 2a<sup>2,3</sup>. The Rashba spin-orbit interaction (SOI)<sup>4,5</sup> in this 2DES enables our method. Metalloporphyrins, cyclic  $\pi$ -conjugated molecules with a centrally hosted metal ion, are actively studied in fields from optoelectronics to spin electronics and sensing, due to the richness of phenomena arising from the interaction of the metal ion and the  $\pi$ -system. Of special biological interest are metalloporphyrins containing iron, such as hemoglobin, myoglobin, and cytochromes, all containing a heme moiety. The spin and local magnetic moment of the iron centers in heme imbue the functional group with many of its properties<sup>6</sup>, and can be used to determine the state of the ion<sup>7–10</sup>. The biophysics interest in the iron centers' spin states and their impact on biological functions is substantial, long-standing<sup>11–12</sup> and ongoing. Hemin-functionalized InAs and InP surfaces *e.g.* act as sensitive sensors for NO<sup>13</sup>. The electronic structure of iron in hemoglobin and hemin in solution indicate a high-spin ferric state<sup>14</sup>. First-principles atomistic calculations<sup>15</sup> of myoglobin bound with different ligands suggests fluctuating magnetic moments in the heme portion, correlated with high- and low-spin states of the iron center. In this work, the labile state of the biologically relevant spin in hemin opens avenues for measuring the spin exchange with nearby electrons in a nanoscale solid-state hybrid device, thereby quantifying the spin state. Like studies may moreover provide the insight to construct bioinspired nanostructured materials using tunable electron systems as intermediary to mediate an exchange between biological entities.

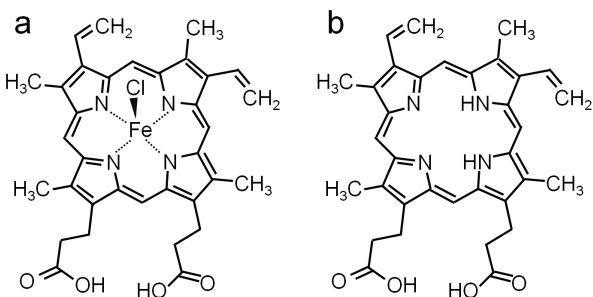


**Figure 1** | Chemical structures of the surface species used in this work. (a), Structure of hemin chloride (hemin), with the Fe center in the +3 oxidation state. (b), Structure of Protoporphyrin IX (PP-IX).

The spin interactions measurably modify the quantum corrections to the 2DES electrical conductivity at low temperatures ( $< 10$  K). The corrections in electronic transport stem from quantum interference of electron partial waves on time-reversed pairs of backscattered trajectories. Constructive interference results in increased backscattering and hence increased resistance (weak localization, WL). Under SOI a closed diffusive path is accompanied by a spin rotation of  $2\pi$ , resulting in a change of sign of the wavefunction, destructive interference, reduced backscattering and hence decreased resistance (antilocalization, AL)<sup>16</sup>. AL thus originates in spin-dependent interference of electrons and is sensitive to spin decoherence<sup>1,16–19</sup>. The spin decoherence of the surface electrons in turn is a sensitive gauge of their spin interactions with magnetic impurities, exceeding direct magnetic measurements in sensitivity<sup>20</sup> and capable of quantifying spin interactions in our low-dimensional spin system. Parallels with magnetic resonance methods (EPR and NMR) can be found in the method of characterizing the local spin environment by measuring the spin decoherence time (a  $T_2$  time). In AL, a magnetic field  $B$  applied normally to the 2DES breaks the time reversal symmetry and reduces the interference effect, leading to a characteristic magnetoresistance (MR)<sup>1,17–19</sup> determined by four characteristic decoherence or scattering rates<sup>1,19,21</sup>. The scattering rates (inverse scattering times) are the elastic scattering rate  $\tau_0^{-1}$  as independently deduced from the areal electron density  $n_s$  and from the electron mobility, the inelastic scattering rate  $\tau_i^{-1}$ , the SOI scattering rate  $\tau_{SO}^{-1}$ , and the magnetic spin-flip scattering rate  $\tau_s^{-1}$ . The total electron decoherence rate,  $\tau_\phi^{-1}$ , is obtained as  $\tau_\phi^{-1} = \tau_i^{-1} + 2\tau_s^{-1}$ . The spin-flip rate  $\tau_s^{-1}$  is here of particular value because it conveys information about the interactions between the surface hemin and the 2DES<sup>1,19</sup>. The experiments measure the longitudinal resistance  $R(B)$ , with data presented as MR,  $\Delta R(B) = R(B) - R(B=0)$  normalized to  $R_0 = R(B=0)$ . Since the quantum corrections to the two-dimensional conductivity  $\sigma_2(B)$  are small, we have  $\Delta R(B)/R_0 \approx -\Delta\sigma_2(B)/\sigma_2(B=0)$  where  $\Delta\sigma_2(B) = \sigma_2(B) - \sigma_2(B=0)$ . This work uses the expression for  $\Delta\sigma_2(B)$  of Ref. 18 modified for the presence of spin-flip scattering<sup>19</sup>:

$$\Delta\sigma_2(B) = -\frac{e^2}{2\pi^2\hbar} \left[ F\left(\frac{B_0}{|B|}\right) - F\left(\frac{B_i + B_{so} + B_s}{|B|}\right) + \frac{1}{2}F\left(\frac{B_i + 2B_s}{|B|}\right) - \frac{1}{2}F\left(\frac{B_i + 2B_{so}}{|B|}\right) \right], \quad (1)$$

where  $F(x) = \Psi(1/2 + x) - \ln(x)$ ,  $\Psi$  is the digamma function, and each scattering time  $\tau_\alpha$  (with  $\alpha = 0, i, so, s$ ) enters via a characteristic magnetic field  $B_\alpha = \hbar/(4eD\tau_\alpha)$ , with  $D$  the two-dimensional diffusion coefficient. A numerical fit of  $\Delta R(B)/R_0$  to equation (1) allows for the extraction of the unknown scattering rates. Expressions derived from Ref. 18 have the advantage of computational simplicity and physical transparency<sup>22</sup>, while assuming a diffusive transport regime, where also the Elliott-Yafet (EY) spin-orbit scattering mechanism<sup>23,24</sup> dominates over the D'yakonov-Perel (DP) mechanism<sup>23,24</sup>,

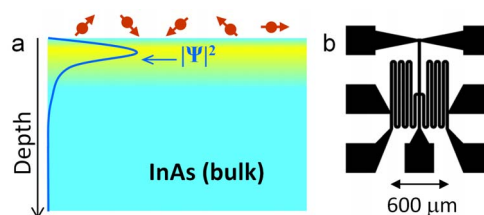


**Figure 2** | 2DES at InAs surface and serpentine pattern. (a), Schematic cross-section of the 2DES electron accumulation layer ( $\sim 20$  nm in depth) at the surface of InAs.  $|\Psi|^2$  represents the electron wavefunction probability density (arbitrary units), maximal  $\sim 8$  nm from the surface, and tailing off into the InAs bulk. The hemin molecules on the surface are represented by red circles, and the spin associated with them as red arrows. (b), Optical photograph of a serpentine pattern, with electrical contact areas. Serpentine mesas are fabricated by photolithography, and are employed to increase the MR signal by increasing the InAs channel length to width ratio.

and have applicability in the low magnetic field regime with  $B < B_0$ . As shown below, the data numerically follows Eq. 1 very closely, while yielding a consistent series of scattering times compatible with physical understanding. More important in this method than absolute values of the  $\tau_\alpha$  is that the relative values of the  $\tau_\alpha$  do not vary significantly with consistent application of the same model. Then reliable information is obtained from the comparative trend under surface coverage by hemin and under varying temperature  $T$ . Consistency of the data with the model is further demonstrated by showing, below, that the behavior of SOI scattering rate  $\tau_{SO}^{-1}$  is compatible with the EY mechanism.

## Results

Hemin is used as a model for hemoglobin, with protoporphyrin IX (PP-IX, Fig. 1b), as the iron-free species. Comparative quantum interference experiments<sup>19</sup> involving PP-IX, hemin, and solvent only, are performed to assess the influence of the iron center. The InAs surface is patterned with serpentine mesas (Fig. 2b) (Supplementary Section 1). Starting with three serpentine, we deposit 0.1  $\mu\text{L}$  of 6  $\mu\text{M}$  solution of PP-IX on one, and of hemin on the second, both in the same ethanol : dichloromethane solvent. The third serpentine is covered by 0.1  $\mu\text{L}$  solvent only, as reference for the comparative study. As the PP-IX and hemin solutions air-dry, they leave behind multilayers of PP-IX or hemin on their respective serpentine. After drying, the three serpentine are cooled-down to measurement temperatures  $T$  ( $0.4 \text{ K} \leq T \leq 5 \text{ K}$ ) at the same time, minimizing cool-down variations. The AL signals are comparatively measured on the three serpentine, and it is from the comparative (rather than absolute) data that conclusions are drawn about the interactions between hemin spins and electron spins. Comparative measurements between serpentine fabricated in parallel and in identical conditions, and with the same processing and cool-down, eliminate variations due to the sensitivity of the InAs 2DES to external factors.

Surface characterization of hemin-functionalized InAs for NO sensing<sup>13</sup> and surface studies of PP-IX on Pt vs ZnPP-IX on Pt<sup>25</sup> suggest that PP-IX and hemin anchor to a metallic surface through the carboxylic groups, predominantly in an upright orientation for PP-IX, although for ZnPP-IX, the molecules were at an angle from the normal to the surface. Several interactions are at play, including chemisorption via the carboxylic groups,  $\pi$ -interaction between protoporphyrins, and electrostatic interaction between the metal ion of the hemin and the 2DES. Atomic force micrographs (Supplementary Section 2) of multilayers of PP-IX and hemin on unpatterned InAs surfaces show differences in aggregation patterns, presumably due to various interactions of the molecules and the surface. The quantum interference measurement is an averaging technique on an ensemble



of surface magnetic moments and hence minimizes effects of local differences in  $n_s$ , surface attachment and orientation.

Figures 3a–c contain MR data due to AL for the three serpentines, presented as  $\Delta R(B)/R_0$ . Data are parametrized in  $T$ , with  $0.4 \text{ K} \leq T \leq 5.0 \text{ K}$ . At lower  $T$  the positive MR for  $B \approx 0$  crosses over to negative MR at higher  $B$ , a characteristic of AL due to SOI beneficial to obtain values for  $\tau_s^{-1}$  since the non-monotonous MR permits unambiguous numerical fits between data and equation (1). The AL correction fades at higher  $T$  due to an increased phase decoherence (quantified below). The data in Figs. 3a–c differ markedly, demonstrating the dependence of AL on specific surface species. The numerical fits of

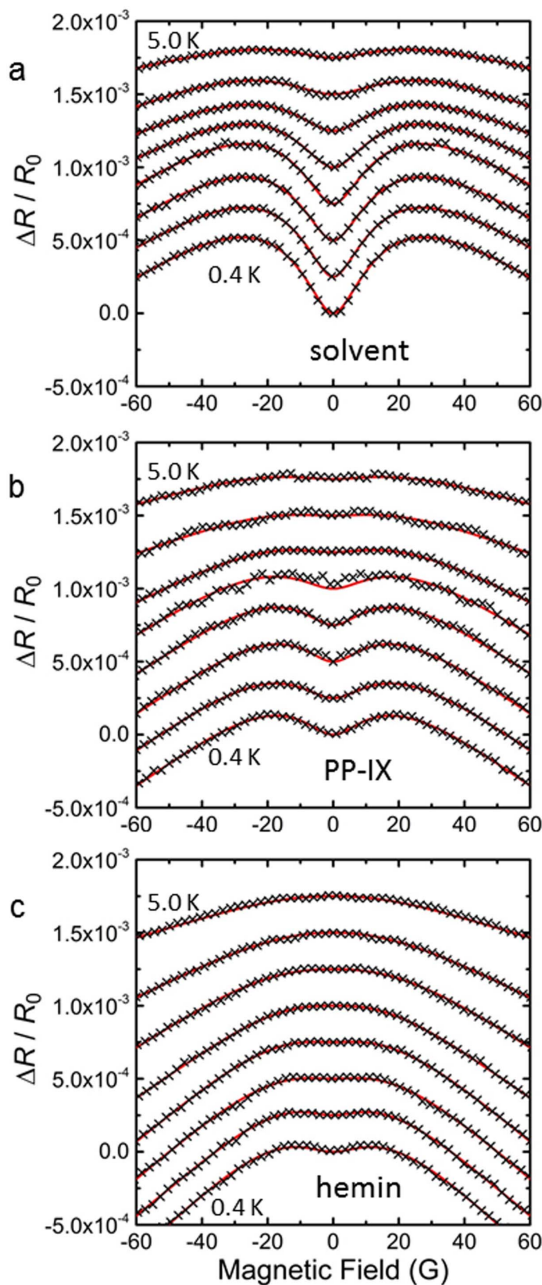


**Figure 3** | Magnetoconductance due to AL for the three serpentines as  $\Delta R(B)/R_0$ , parametrized in  $T$ . (a), Solvent-covered serpentine. (b), PP-IX-covered serpentine. (c), Hemin-covered serpentine. In each panel the 8 curves are offset by  $2.5 \times 10^{-4}$ . Each curve represents data at different  $T$ ; from low to high,  $T = 0.4, 0.55, 0.70, 0.85, 1.2, 2.0, 3.0, 5.0 \text{ K}$ . Black crosses represent experimental data, out of which 1 in 10 is plotted for clarity. Solid red lines are best numerical fits to equation (1).

the data in Fig. 3 to equation (1) were realized using the Monte-Carlo based cross-entropy method<sup>26,27</sup> (Supplementary Section 4), which is well-adapted to non-linear multi-extremal optimization problems in a multi-parameter space. Figure 3 shows an excellent correspondence between the data and Eq. 1. The fitting parameters are  $B_i$ ,  $B_{so}$  and  $B_s$  (proportional to the corresponding scattering rates), while the elastic scattering field  $B_0$  is determined from the measured  $n_s$  and mobility in the 2DES (Methods, and Supplementary Section 3). Uniqueness of the numerical fits is aided by the characteristic cross-over from positive MR to negative MR, here occurring for  $B \approx 20 \text{ G}$ . Equation 1 assumes a range of  $B$  not exceeding  $B_0$ . From the transport parameters (Supplementary Section 3), the average of  $B_0$  over serpentines and over  $T$  can be estimated as  $B_0 \approx 32 \text{ G}$ . Thus the range of  $B$  most determining for the fits is included in theoretical region of validity of Eq. 1, supporting the consistency between model and data. In Eq. 1  $B_i$ ,  $B_{so}$  and  $B_s$  appear as combinations  $B_{so} - B_s$  (corresponding to an effective spin scattering rate) and  $B_i + 2B_s$  (corresponding to  $\tau_\phi^{-1}$ ) such that only two of the unknown fields can be determined from one data set and an added constraint is necessary<sup>19,28</sup>. We consider that  $B_s = 0$  for the reference solvent-covered serpentine, where no magnetic scattering centers are introduced on the 2DES, and therefore values for  $B_i$  and  $B_{so}$  can be determined. For PP-IX- and hemin-covered serpentines, we assume that  $\tau_i^{-1}$  (from which  $B_i$  is determined) is unchanged from the solvent-covered serpentine. These assumptions have precedents in the literature<sup>1,19,28</sup> and are justified from the knowledge that in metal systems magnetic impurities lead to an increase in magnetic spin-flip and SOI scattering rates but leave inelastic scattering unaffected. The identical processing and cool-down history of the serpentines helps validate this assumption, as does the resulting excellence of the fits. With  $B_i$  provided by the reference measurement,  $B_{so}$  and  $B_s$  can be determined for the PP-IX- and hemin-covered serpentines to determine the change induced in spin-orbit and spin-flip scattering by the addition of the surface species. Below we discuss the various extracted scattering rates vs  $T$ , all presented in Fig. 4. Error bars in Fig. 4 take into account the sensitivity of the fitting residue to a variation in the  $B_x$ .

## Discussion

We start with the inelastic scattering rates  $\tau_i^{-1}$  (Fig. 4a) which show a dependence on  $T$  close to linear. By the procedure above, the values of  $\tau_i^{-1}$  are unchanged between the PP-IX-, hemin-, and solvent-covered serpentines. The data can be fitted to  $\tau_i^{-1} = AT^{1.02} + \tau_{sat}^{-1}$  over the measurement range ( $A$  and  $\tau_{sat}^{-1}$  are fitting parameters). For low-dimensional systems at low  $T$ , Nyquist decoherence<sup>21,29</sup> originating in fluctuations in the electromagnetic background often determines  $\tau_i^{-1}$ , and in two dimensions results in  $\tau_i^{-1} \sim T$ , consistent with the present measurements. The term  $\tau_{sat}^{-1}$  denotes a low- $T$  saturation of phase coherence, frequently observed while not fully understood<sup>21</sup>. In this measurement  $\tau_{sat} \approx 19 \text{ ps}$ , constituting an upper bound for  $\tau_i$ .

The spin-orbit scattering rates  $\tau_{so}^{-1}$  contained in Fig. 4b convey the relative strength of SOI among the differently-covered serpentines. Within the error bars, the non-monotonic dependence on  $T$  tracks the dependence of  $n_s$  and mobility in the 2DES (Supplementary Section 3) and can be used to qualitatively identify the dominant spin-orbit scattering mechanism. In the EY mechanism a momentum scattering event leads to a spin-orbit scattering event due to spin-momentum locking, and a dependence  $\tau_{so}^{-1} \sim E_F^2/\tau_0$  is expected<sup>23,24</sup>, where  $E_F$  denotes the Fermi level. Hence in a 2DES with constant density-of-states, the EY mechanism leads to  $\tau_{so}^{-1} \sim n_s^2/\tau_0$ . In the DP mechanism spin-orbit scattering is mitigated by motional narrowing and  $\tau_{so}^{-1} \sim n_s^3 \tau_0$  is expected<sup>23,24</sup>. Experimentally, minima are observed in  $\tau_{so}^{-1}$ ,  $n_s$  and  $\tau_0$ , at  $T \approx 1.2 \dots 2 \text{ K}$ , and the highest measured values occur at  $T \approx 5 \text{ K}$ . The ratio between low and high values for  $n_s^2/\tau_0$  is approximately 0.60, for  $n_s^3 \tau_0$  approximately 0.35, and for  $\tau_{so}^{-1}$  approximately 0.69. From

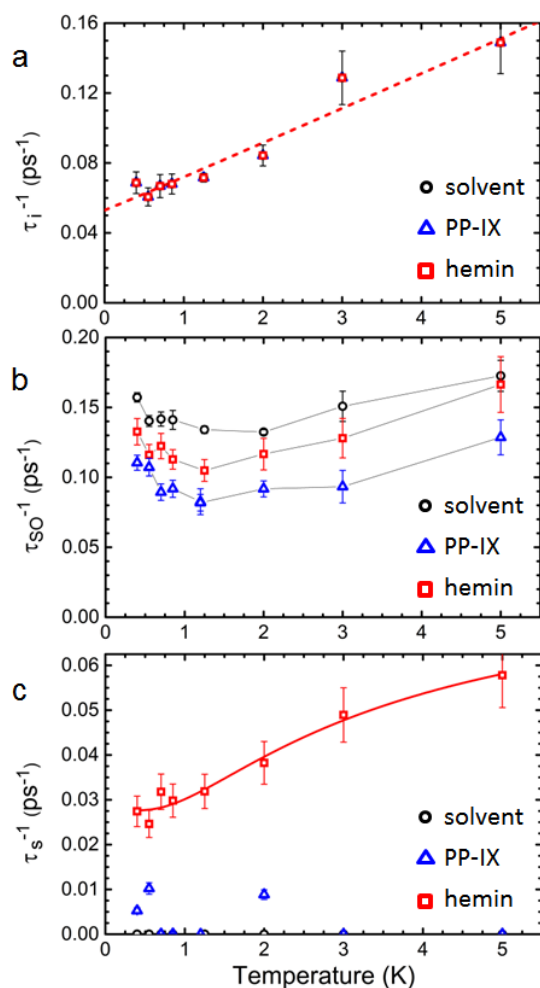


**Figure 4** | Scattering rates as function of  $T$ . (a), The inelastic scattering rates  $\tau_i^{-1}$ . (b), The SOI scattering rates  $\tau_{SO}^{-1}$ . (c), The magnetic spin-flip scattering rates  $\tau_s^{-1}$ . In each panel black circles represent scattering rates for the solvent-covered serpentine, blue triangles for the PP-IX-covered serpentine, and red squares for the hemin-covered serpentine. In (a) the dashed red line represents a best fit to  $\tau_i^{-1} \sim T^{1.02}$ , and in (c) the solid red line represents a best fit to  $\tau_s^{-1} = \tau_{\Delta s}^{-1} + (\tau_{if}^{-1}) \exp(-E_a/k_B T)$ , both as discussed in the text. In (b) the lines connecting data for  $\tau_{SO}^{-1}$  form guides to the eye only. Error bars are indicated by vertical lines.

the ratios it is apparent that the EY mechanism provides a better description for spin-orbit scattering in this system than does the DP mechanism, as expected for a system where mobility is adversely impacted by its proximity to an exposed surface. The EY mechanism limiting  $\tau_{SO}^{-1}$  is consistent with the use of Eq. 1. With the EY mechanism limiting  $\tau_{SO}^{-1}$ , it is further expected that  $B_{so}$  will be less sensitive to the surface electric field<sup>24</sup>, an advantage for the present method. Indeed in the InAs surface system the electric field is not well controlled and a large randomness in the combination  $B_{so} - B_s$ , from which the magnetic spin-flip rate  $\tau_s^{-1}$  is determined, would also have induced additional uncertainty in  $\tau_s^{-1}$ .

Compared to the solvent-covered serpentine, PP-IX and hemin reduce  $\tau_{SO}^{-1}$  and concomitantly reduce the SOI experienced in the 2DES, by  $\sim 35\%$  for PP-IX and  $\sim 15\%$  for hemin. The relative reduction in  $\tau_{SO}^{-1}$  for PP-IX and hemin is maintained over the range of  $T$  and hence consistently points to an influence of surface coverage. The origin of the decrease must be searched for in the electrostatic interactions between the surface entities and the metallic 2DES. The delocalized electrons associated with the cyclic conjugated groups in the PP-IX molecules are expected to induce a shielding

of the surface electric field, diminishing inversion asymmetry and SOI. The same effect will occur under hemin coverage, with same overall organic structure as PP-IX. However, the presence of the Fe center of higher atomic weight will increase the average SOI experienced by electrons in its proximity, an effect also observed in metals systems with adatoms<sup>19,30</sup>. The effect will diminish the reduction in SOI relative to PP-IX, as indeed observed.

Figure 4c contains the magnetic spin-flip rates  $\tau_s^{-1}$ . Within the error bars, the data show that spin-flip scattering is low in the PP-IX-covered serpentine and substantial in the hemin-covered serpentine where furthermore a distinct  $T$ -dependence is observed. The low values of  $\tau_s^{-1}$  for PP-IX coverage can be understood from the lack of magnetic moment in the molecule. The origin of magnetic spin-flip scattering indeed lies in spin-spin interaction between magnetic moments and the electron spin. An important difference derives from the Fe center in hemin, where a spin exchange mechanism induces substantial spin-flip scattering in the 2DES. The magnitude and  $T$ -dependence of  $\tau_s^{-1}$  implies an interaction  $\sigma \cdot S$  between the hemin local moments  $S$  and electrons spin  $\sigma$ , with  $S$  denoting the total spin of the hemin's  $Fe^{+3}$  ion 3d electrons. The existence of spin-flips in the 2DES moreover implies a change in  $S$ . In hemin's  $Fe^{+3}$  ion, the spin state of the 3d electrons is affected by the surrounding ligands. A strong-field ligand favors pairing of the electrons to form a low-spin  $S=1/2$  state ( ${}^2T_{2g}$ ) while a weak-field ligand favors unpaired electrons forming a high-spin  $S=5/2$  state ( ${}^6A_{1g}$ )<sup>7,9,31</sup>. For a given  $Fe^{+3}$  in hemin, different near-degenerate spin states can occur, resulting in thermal mixtures<sup>8,10,15,31,32</sup>. Moreover, quantum-mechanical mixed-spin ground states are also possible<sup>9</sup>. Further, the magnetic susceptibility of polycrystalline hemin has been observed to follow ferromagnetic behavior, with a Curie-Weiss temperature  $\sim 32$  K, although fully developed magnetization and long-range order were not observed<sup>31</sup>. Since the Curie-Weiss temperature is well above the present measurement range, paramagnetic behavior may be excluded as the origin for the  $T$ -dependence of  $\tau_s^{-1}$ . A more likely origin lies in the occurrence of two labile spin states,  $S = 1/2$  and  $5/2$ , observed previously<sup>32</sup>, due to ligand effects in the solid-state environment possibly fluctuating and leading to transiently quasi-degenerate spin states. Spin exchange interactions with the InAs surface electrons then mediate transitions between finely split energy states of the  $Fe^{+3}$  ion, leading to the observed increase in spin-flip scattering over that observed for PP-IX coverage, and to the  $T$ -dependence of  $\tau_s^{-1}$ . Although the detailed physics differs, the process can be mapped on a model<sup>33</sup> for the rate of magnetization reversal of 2-state superparamagnetic particles with an anisotropy energy barrier (Néel-Brown expression<sup>34</sup>), leading to an expression  $\tau_s^{-1} = \tau_{\Delta s}^{-1} + (\tau_{if}^{-1}) \exp(-E_a/k_B T)$ , where in this case  $E_a$  denotes the average energy difference between the system with  $Fe^{+3}$  in the low-spin vs high-spin state,  $\tau_{if}^{-1}$  is the transition frequency, and  $\tau_{\Delta s}^{-1}$  is included to take into account any  $T$ -independent spin-flip rate of processes unrelated to the  $Fe^{+3}$  mixed spin state. The hemin data can be fitted to the above expression over the measurement range, as depicted in Fig. 4c, and the resulting parameters acquire reasonable values:  $E_a \approx 0.27$  meV,  $\tau_{if}^{-1} \approx 0.057$  ps $^{-1}$ , and  $\tau_{\Delta s}^{-1} \approx 0.028$  ps $^{-1}$ . The low  $E_a$  indeed indicates near-degenerate levels, while  $\tau_{if}^{-1}$  of the same approximate magnitude as the actually measured  $\tau_s^{-1}$  validates the physical picture, and the low  $\tau_{\Delta s}^{-1}$  implies that the labile spin state of  $Fe^{+3}$  plays an important role in the 2DES spin flip scattering. The increase in  $\tau_s^{-1}$  in the presence of hemin compared to solvent or PP-IX indicates the existence of spin interaction between the  $Fe^{+3}$  and the 2DES, serving as example of an artificially constructed structure where a nanoscale solid-state system and a biologically relevant moiety interact.

To conclude, in a bio-organic/semiconductor device a quantum interference measurement was used to quantify the spin interactions between a low-dimensional solid-state electron system and hemin. Antilocalization as a probe of spin decoherence allowed measure-



ments akin to magnetic resonance techniques. The study points towards more active hybrid systems, where bioinspired functional hybrid materials use quantum-mechanical paths available in solid-state systems to achieve interactions between proximate biological entities.

## Methods

**Sample preparation.** All chemicals were used as received. From Sigma-Aldrich, protoporphyrin-IX (PP-IX in text), empirical formula  $C_{34}H_{34}N_4O_4$ , product number P8293, and hemin chloride (hemin) from porcine, empirical formula  $C_{34}H_{32}ClFeN_4O_4$ , product number 51280, were purchased. Dichloromethane was HPLC grade and obtained from CM Science, while 95% denatured ethanol was purchased from EMD. Serpentine patterns were fabricated by photolithography (Supplementary Section 1). The hybrid bio-organic/semiconductor structures were generated by depositing hemin and PP-IX solution onto serpentine patterns. Equal number of moles of PP-IX and hemin are dissolved in the same solvent which is a 1 : 1 ethanol : dichloromethane mixture, yielding 6  $\mu$ M solutions. 0.1  $\mu$ L each of PP-IX, hemin and solvent only are deposited on 3 serpentine patterns, air-dried, and subsequently cooled down and measured.

**Magnetotransport measurements and analysis.** Low temperature magnetotransport measurements were performed in a  $^3$ He cryogenic system equipped with a superconducting magnet. The system has a base temperature of 0.35 K. Localization measurements were achieved in 4-contact low-frequency ac mode, under low current excitation of 20 nA rms to prevent heating of the electronic system. The InAs samples host two types of carriers, namely surface 2DES electrons and bulk electrons. Surface and bulk electrons' densities and mobilities need to be determined, as the presence of multiple carriers results in a classical background in magnetoresistance that has to be subtracted to yield the localization quantum correction, and as the surface electron density and mobility is required to calculate the elastic scattering field  $B_0$ . Measurements of longitudinal and Hall resistance vs  $B$  allowed this characterization of surface and bulk electrons densities and mobilities over  $T$  via fitting to a two-carrier model of classical magnetoresistance, as described in Supplementary Section 3.

- Bergmann, G. Weak localization and its applications as an experimental tool. *Int. J. Mod. Phys. B* **24**, 2015–2052 (2010).
- Tsui, D. C. Landau-level spectra of conduction electrons at an InAs surface. *Phys. Rev. B* **12**, 5739–5748 (1975).
- Mochizuki, T., Masutomi, R. & Okamoto, T. Evidence for two-dimensional spin-glass ordering in submonolayer Fe films on cleaved InAs surfaces. *Phys. Rev. Lett.* **101**, 267204 1–4 (2008).
- Schierholz, C., Matsuyama, T., Merkt, U. & Meier, G. Weak localization and spin splitting in inversion layers on  $p$ -type InAs. *Phys. Rev. B* **70**, 233311 1–4 (2004).
- Matsuyama, T., Kürsten, R., Meißner, C. & Merkt, U. Rashba spin splitting in inversion layers on  $p$ -type bulk InAs. *Phys. Rev. B* **61**, 15588–15591 (2000).
- Poulos, T. L. Heme Enzyme Structure and Function. *Chem. Rev.* **114**, 3919–3962 (2014).
- Ali, Md., E., Sanyal, B. & Oppeneer, P. M. Electronic structure, spin-states, and spin-crossover reaction of heme-related Fe-porphyrins: a theoretical perspective. *J. Phys. Chem. B* **116**, 5849–5859 (2012).
- Atak, K. *et al.* Electronic structure of hemin in solution studied by resonant x-ray emission spectroscopy and electronic structure calculations. *J. Phys. Chem. B* **118**, 9938–9943 (2014).
- Maltempo, M. M. Magnetic state of an unusual bacterial heme protein. *J. Chem. Phys.* **61**, 2540–2547 (1974).
- Mitra, S., Marathe, V. R. & Birdy, R. Magnetic behaviour of spin-mixed iron(III) porphyrins. *Chem. Phys. Lett.* **96**, 103–107 (1983).
- Pauling, L. & Coryell, C. D. The magnetic properties and structure of hemoglobin, oxyhemoglobin and carbonmonoxyhemoglobin. *Proc. Natl. Acad. Sci.* **22**, 210–216 (1936).
- Messana, C. *et al.* Influence of quaternary structure of the globin on thermal spin equilibria in different methemoglobin derivatives. *Biochemistry* **17**, 3652–3662 (1978).
- García, M. A. *et al.* Functionalization and characterization of InAs and InP surfaces with hemin. *J. Vac. Sci. Technol. B* **25**, 1504–1510 (2007).
- Aziz, E. F. *et al.* Probing the electronic structure of the hemoglobin active center in physiological solutions. *Phys. Rev. Lett.* **102**, 0681031 1–4 (2009).
- Weber, C., Cole, D. J., O'Regan, D. D. & Payne, M. C. Renormalization of myoglobin-ligand binding energetics by quantum many-body effects. *Proc. Natl. Acad. Sci.* **111**, 5790–5795 (2014).
- Bergmann, G. Weak anti-localization—An experimental proof for the destructive interference of rotated spin  $\frac{1}{2}$ . *Solid State Commun.* **42**, 815–817 (1982).
- Gang, T. *et al.* Tunable doping of a metal with molecular spins. *Nat. Nanotechnol.* **7**, 232–236 (2012).
- Hikami, S., Larkin, A. I. & Nagaoka, Y. Spin-orbit interaction and magnetoresistance in the two dimensional random system. *Prog. Theor. Phys.* **63**, 707–710 (1980).
- Zhang, Y., Kallaher, R. L., Soghomonian, V. & Heremans, J. J. Measurement by antilocalization of interactions between InAs surface electrons and magnetic surface species. *Phys. Rev. B* **87**, 054430 1–6 (2013).
- Mallet, F. *et al.* Scaling of the low-temperature dephasing rate in Kondo systems. *Phys. Rev. Lett.* **97**, 226804 1–4 (2006).
- Lin, J. J. & Bird, J. P. Recent experimental studies of electron dephasing in metal and semiconductor mesoscopic structures. *J. Phys.: Condens. Matter* **14**, R501–R596 (2002).
- McPhail, S. *et al.* Weak localization in high-quality two-dimensional systems. *Phys. Rev. B* **70**, 245311 1–16 (2004).
- Song, P. H. & Kim, K. W. Spin relaxation of conduction electrons in bulk III-V semiconductors. *Phys. Rev. B* **66**, 035207 1–8 (2002).
- Litvinenko, K. L., Murdin, B. N. & Allam, J. *Phys. Rev. B* **74**, 075331 1–6 (2006).
- Humbert, C. *et al.* On the protoporphyrin monolayers conformation. *Chem. Phys. Chem.* **7**, 569–571 (2006).
- Kroese, D. P., Porotsky, S. & Rubinstein, R. Y. The cross-entropy method for continuous multi-extremal optimization. *Methodol. Comput. App.* **8**, 383–407 (2006).
- Peres, M. L. *et al.* Experimental investigation of spin-orbit coupling in  $n$ -type PbTe quantum wells. *J. Appl. Phys.* **115**, 093704 1–6 (2014).
- Wei, W. & Bergmann, G. CuCo: A new surface Kondo system. *Phys. Rev. B (RC)* **37**, 5990–5993 (1988).
- Altshuler, B. L., Aronov, A. G. & Khmel'nitsky, D. E. Effects of electron-electron collisions with small energy transfers on quantum localization. *J. Phys. C* **15**, 7367–7386 (1982).
- Bergmann, G. Weak localization in thin films: a time-of-flight experiment with conduction electrons. *Phys. Rep.* **107**, 1–58 (1984).
- Owens, J. W., Robinson, J. & O'Connor, Ch. J. The behavior of ferric protoporphyrin-IX in alkaline DMF. *Inorg. Chim. Acta.* **206** 141–153 (1993).
- Bartoszek, M., Balandab, M., Skrzypeka, D. & Drzazgaa, Z. Magnetic field effect on hemin. *Physica B* **307**, 217–223 (2001).
- Mørup, S., Madsen, D. E., Frandsen, C., Bahl, C. R. H. & Hansen, M. F. Experimental and theoretical studies of nanoparticles of antiferromagnetic materials. *J. Phys.: Condens. Matter* **19**, 213202–213233 (2007).
- Wernsdorfer, W. *et al.* Experimental evidence of the Néel-Brown model of magnetization reversal. *Phys. Rev. Lett.* **78**, 1791–1794 (1997).

## Acknowledgments

The work was supported by the U.S. Department of Energy, Office of Basic Energy Sciences, Division of Materials Sciences and Engineering, under Award no. DOE DE-FG02-08ER46532.

## Author contributions

V.D. fabricated the InAs samples, performed the AL measurements, and analyzed the data. Y.Z. aided in the sample fabrication and measurement. V.S. and J.J.H. conceived and designed the experiments, interpreted the results and wrote the manuscript. All authors discussed the results and commented on the manuscript.

## Additional information

Supplementary information accompanies this paper at <http://www.nature.com/scientificreports>

**Competing financial interests:** The authors declare no competing financial interests.

**How to cite this article:** Deo, V., Zhang, Y., Soghomonian, V. & Heremans, J.J. Quantum interference measurement of spin interactions in a bio-organic/semiconductor device structure. *Sci. Rep.* **5**, 9487; DOI:10.1038/srep09487 (2015).



This work is licensed under a Creative Commons Attribution 4.0 International License. The images or other third party material in this article are included in the article's Creative Commons license, unless indicated otherwise in the credit line; if the material is not included under the Creative Commons license, users will need to obtain permission from the license holder in order to reproduce the material. To view a copy of this license, visit <http://creativecommons.org/licenses/by/4.0/>